would also be needed, to keep the outside surface of the sensor at room temperature.

Our magnetometer is in a very early stage of development, and many improvements are possible. For example, by using a two-dimensional photodiode array it should be possible to measure gradients and localize sources in two directions. The overall noise of the magnetometer could be further reduced by using superconducting shields, which do not have a Johnson noise component. In the absence of Johnson noise, simple averaging of the existing channels would yield a sensitivity of 0.2 fT $Hz^{-1/2}$. With more optimization, such as increased probe laser power and increased K atom density, it should be possible to approach the shot-noise-limited sensitivity in the range 10^{-2}–10^{-3} fT $Hz^{-1/2}$. The thermal magnetic noise produced by the brain[25] is of the order of 0.1 fT $Hz^{-1/2}$, so an optimized version of this magnetometer should enable the maximum possible amount of information to be obtained about brain electrical activity. This may enable non-invasive studies of individual cortical modules in the brain[26], which have a size of 0.1–0.2 mm. □

Received 24 October 2002; accepted 4 February 2003; doi:10.1038/nature01484.

1. Weinstock, H. (ed.) *SQUID Sensors: Fundamentals, Fabrication and Applications* (Kluwer Academic, Dordrecht, 1996).
2. Aleksandrov, E. B. *et al.* Laser pumping in the scheme of an M_x-magnetometer. *Optics Spectrosc.* **78,** 292–298 (1995).
3. Budker, D., Kimball, D. F., Rochester, S. M., Yashchuk, V. V. & Zolotorev, M. Sensitive magnetometry based on non-linear magneto-optical rotation. *Phys. Rev. A* **62,** 043403 (2000).
4. Affolderbach, C., Stähler, M., Knappe, S. & Wynands, R. An all-optical, high sensitivity magnetic gradiometer. *Appl. Phys. B* **75,** 605–612 (2002).
5. Tsuei, C. C. & Kirtley, J. R. Phase-sensitive evidence for d-wave pairing symmetry in electron-doped cuprate superconductors. *Phys. Rev. Lett.* **85,** 182–185 (2000).
6. Harry, G. M., Jin, I., Paik, H. J., Stevenson, T. R. & Wellstood, F. C. Two-stage superconducting-quantum-interference-device amplifier in a high-Q gravitational wave transducer. *Appl. Phys. Lett.* **76,** 1446–1448 (2000).
7. Greenberg, Ya. S. Application of superconducting quantum interference devices to nuclear magnetic resonance. *Rev. Mod. Phys.* **70,** 175–222 (1998).
8. McDermott, R. *et al.* Liquid-state NMR and scalar couplings in microtesla magnetic fields. *Science* **295,** 2247–2249 (2002).
9. Kirschvink, J. L., Maine, A. T. & Vali, H. Paleomagnetic evidence of a low-temperature origin of carbonate in the Martian meteorite ALH84001. *Science* **275,** 1629–1633 (1997).
10. Tralshawala, N., Claycomb, J. R. & Miller, J. H. Practical SQUID instrument for non-destructive testing. *Appl. Phys. Lett.* **71,** 1573–1575 (1997).
11. Clem, T. R. Superconducting magnetic gradiometers for underwater target detection. *Naval Engineers J.* **110,** 139–149 (1998).
12. Hämäläinen, M. *et al.* Magnetoencephalography—theory, instrumentation, and applications to non-invasive studies of the working human brain. *Rev. Mod. Phys.* **65,** 413–497 (1993).
13. Rodriguez, E. *et al.* Perception's shadow: long-distance synchronization of human brain activity. *Nature* **397,** 430–433 (1999).
14. Zimmerman, J. E., Thiene, P. & Harding, J. T. Design and operation of stable RF-biased superconducting point-contact quantum devices, and a note on properties of perfectly clean metal contacts. *J. Appl. Phys.* **41,** 1572–1580 (1970).
15. Drung, D., Bechstein, S., Franke, K. P., Scheiner, M. & Schurig, T. Improved direct-coupled dc SQUID read-out electronics with automatic bias voltage tuning. *IEEE Trans. Appl. Supercond.* **11,** 880–883 (2001).
16. Oukhanski, N., Stolz, R., Zakosarenko, V. & Meyer, H. G. Low-drift broadband directly coupled dc SQUID read-out electronics. *Physica C* **368,** 166–170 (2002).
17. Del Gratta, C., Pizzella, V., Tecchio, F. & Romani, G. L. Magnetoencephalography—a noninvasive brain imaging method with 1 ms time resolution. *Rep. Prog. Phys.* **64,** 1759–1814 (2001).
18. Nenonen, J., Montonen, J. & Katila, T. Thermal noise in biomagnetic measurements. *Rev. Sci. Instrum.* **67,** 2397–2405 (1996).
19. Dupont-Roc, J., Haroche, S., Cohen-Tannoudji, C. Detection of very weak magnetic fields (10^{-9} gauss) by ^{87}Rb zero-field level crossing resonances. *Phys. Lett. A* **28,** 638–639 (1969).
20. Budker, D. *et al.* Resonant nonlinear magneto-optical effects in atoms. *Rev. Mod. Phys.* **74,** 1153–1201 (2002).
21. Allred, J. C., Lyman, R. N., Kornack, T. W. & Romalis, M. V. High-sensitivity atomic magnetometer unaffected by spin-exchange relaxation. *Phys. Rev. Lett.* **89,** 130801 (2002).
22. Budker, D., Yashchuk, V. & Zolotorev, M. Nonlinear magneto-optic effects with ultra-narrow widths. *Phys. Rev. Lett.* **81,** 5788–5791 (1998).
23. Alexandrov, E. B., Balabas, M. V., Pasgalev, A. S., Vershovskii, A. K. & Yakobson, N. N. Double-resonance atomic magnetometers: From gas discharge to laser pumping. *Laser Phys.* **6,** 244–251 (1996).
24. Kandori, A., Miyashita, T. & Tsukada, K. Cancellation technique of external noise inside a magnetically shielded room used for biomagnetic measurements. *Rev. Sci. Instrum.* **71,** 2184–2190 (2000).
25. Varpula, T. & Poutanen, T. Magnetic field fluctuations arising from thermal motion of electric charge in conductors. *J. Appl. Phys.* **55,** 4015–4021 (1984).
26. Ts'o, D. Y., Frostig, R. D., Lieke, E. E. & Grinvald, A. Functional organisation of primate visual cortex revealed by high-resolution optical imaging. *Science* **249,** 417–420 (1990).
27. Happer, W. & Tam, A. C. Effect of rapid spin exchange on the magnetic-resonance spectrum of alkali vapors. *Phys. Rev. A* **16,** 1877–1991 (1977).

Acknowledgements This work was supported by the NIH, the Packard Foundation and Princeton University.

Competing interests statement The authors declare that they have no competing financial interests.

Correspondence and requests for materials should be addressed to M.R. (e-mail: romalis@princeton.edu).

Single-crystal gallium nitride nanotubes

Joshua Goldberger*, Rongrui He*, Yanfeng Zhang†, Sangkwon Lee†, Haoquan Yan*, Heon-Jin Choi† & Peidong Yang*†

* *Department of Chemistry, University of California, Berkeley, California 94720, USA*

† *Materials Science Division, Lawrence Berkeley National Laboratory, Berkeley, California 94720, USA*

Since the discovery of carbon nanotubes in 1991 (ref. 1), there have been significant research efforts to synthesize nanometre-scale tubular forms of various solids[2–10]. The formation of tubular nanostructure generally requires a layered or anisotropic crystal structure[2–4]. There are reports[5,6,11] of nanotubes made from silica, alumina, silicon and metals that do not have a layered crystal structure; they are synthesized by using carbon nanotubes and porous membranes as templates, or by thin-film rolling. These nanotubes, however, are either amorphous, polycrystalline or exist only in ultrahigh vacuum[8]. The growth of single-crystal semiconductor hollow nanotubes would be advantageous in potential nanoscale electronics, optoelectronics and biochemical-sensing applications. Here we report an 'epitaxial casting' approach for the synthesis of single-crystal GaN nanotubes with inner diameters of 30–200 nm and wall thicknesses of 5–50 nm. Hexagonal ZnO nanowires were used as templates for the epitaxial overgrowth of thin GaN layers in a chemical vapour deposition system. The ZnO nanowire templates were subsequently removed by thermal reduction and evaporation, resulting in ordered arrays of GaN nanotubes on the substrates. This templating process should be applicable to many other semiconductor systems.

We grew arrays of ZnO nanowires on (110) sapphire wafers using a vapour deposition process developed in our laboratory[12]. These ZnO nanowire arrays were placed inside a reaction tube for GaN chemical vapour deposition. Trimethylgallium and ammonia were used as precursors, and were fed into the system with argon or nitrogen carrier gas. The deposition temperature was set at 600–700 °C. After the GaN deposition, the samples were treated at 600 °C with 10% H_2 in argon to remove the ZnO nanowire templates.

Figure 1a shows a scanning electron microscopy (SEM) image of the starting ZnO nanowire array templates. These nanowires have uniform lengths of 2–5 μm and diameters of 30–200 nm. They are well facetted with hexagonal cross-sections (Fig. 1a inset), exhibiting {110} planes on the sides. After the GaN deposition and template removal, the colour of the sample turns from white to yellowish or darker. The morphology of the initial nanowire arrays was maintained (Fig. 1b), except for the increase in the diameters of the resulting nanostructures. The nanostructures appear less facetted than the starting ZnO nanowire template. Compositional analysis on the final product shows little Zn signal. X-ray diffraction (XRD) on the sample shows only (00*l*) diffraction peaks of the

wurtzite GaN structure (Fig. 1c), which indicates excellent epitaxy/texturing for the GaN coating.

The sample in Fig. 1b was dispersed onto a transmission electron microscopy (TEM) grid for further structural analysis. It was found that most of the nanostructures exhibit tubular structures with uniform wall thicknesses (Fig. 2a). The nanotubes have inner diameters ranging from 30 to 200 nm, similar to the ZnO nanowire arrays, and wall thicknesses between 5 and 50 nm (Fig. 2a–c). Most of the tubes have only one end open, but some tubes with both ends open were also observed. Figure 2a–c shows representative images of these GaN nanotubes. These observations are consistent with our SEM studies, where round and less-facetted ends are observed after the GaN coating (Fig. 1b). We thus conclude that those open nanotube ends were originally located at the GaN and substrate interface, and were broken open during TEM sample preparation. Indeed, we have frequently observed these open ends on the substrate surface together with the corresponding nanotubes (Fig. 1b inset). TEM studies also indicate that the inner cross-section of the nanotubes remains pseudo-hexagonal after the template removal (Supplementary Information).

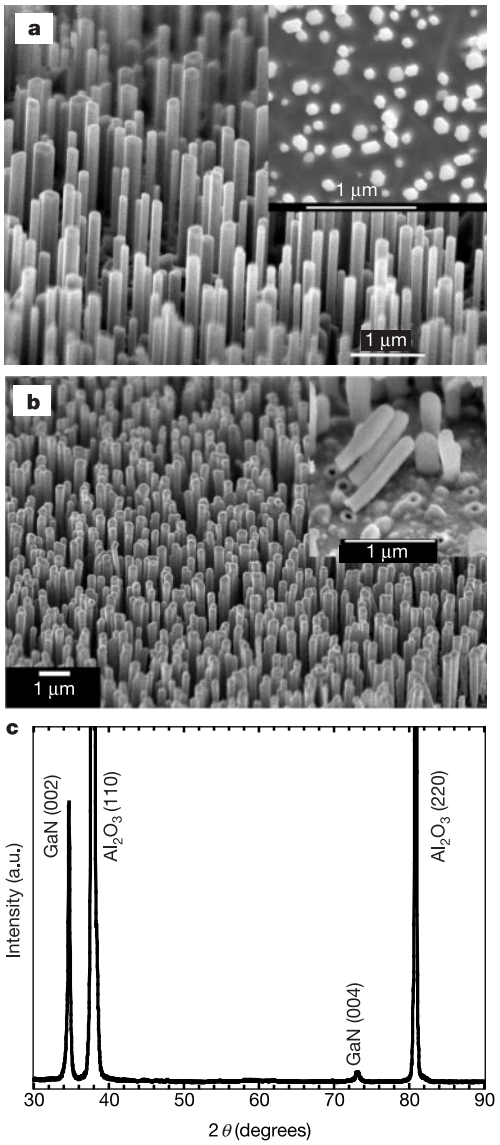

Figure 1 Arrays of ZnO nanowires and GaN nanotubes. Shown are SEM images of the ZnO nanowire template arrays (**a**), and the resulting GaN nanotube array (**b**). Inset in **a** shows cross-sections of the ZnO nanowires. Inset in **b** shows the fractured interface between the GaN nanotubes and the substrate. **c**, XRD of the GaN nanowire array.

Electron diffraction measurements on these GaN nanotubes indicates that they are single crystals. Figure 2e inset shows one such diffraction pattern taken along the [$\bar{1}$10] zone axis. It can be readily seen that the nanotube is oriented along the *c* axis of the wurtzite GaN structure. This is consistent with the XRD data, where only (00*l*) peaks were observed. Along the tube axis, a lattice spacing of 0.51 nm for (001) planes of the wurtzite structure can be readily resolved on high-resolution TEM images of both the tube surface (Fig. 2d) and the inside of the tubes (Fig. 2e).

Compositional line profiles probed by energy dispersive X-ray spectroscopy (EDX) shows well-correlated gallium and nitrogen signals across the tube walls (Fig. 2f), indicating stoichiometric GaN formation during the deposition. This is also clearly reflected in the

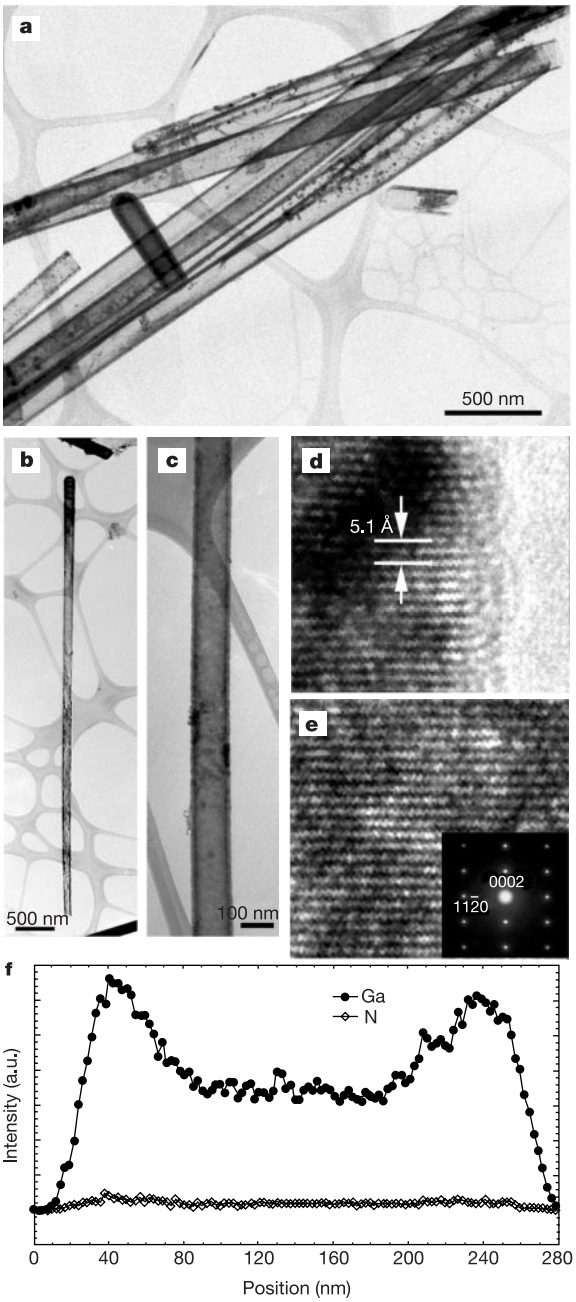

Figure 2 Structural characterization of GaN nanotubes. **a**–**c**, TEM images of the GaN nanotubes (**a**–**c**). **d**, High-resolution TEM images of a GaN nanotube wall at the surface, and **e**, the inside of the tube. Inset in **e** is an electron-diffraction pattern of the nanotube along the [$\bar{1}$10] zone axis. **f**, Compositional line profile across the nanotube probed by EDX spectroscopy.

electron energy loss spectra recorded on these nanotubes, where strong nitrogen signals were observed (Supplementary Information). We note that the interfacial diffusion between the GaN layer and the ZnO nanowire templates results in a small amount of Zn or O incorporation within the GaN tube wall.

Taken together, the above measurements show that we have successfully prepared high-density arrays of single-crystal GaN nanotubes on sapphire substrates. We point out that the GaN nanotube formation reported here differs from all previous work on inorganic nanotubes[1–6]. Most of the previous studies on inorganic nanotubes have been on materials with layered structures (for example, VO_x, MoS_2, $NiCl_2$, BN)[1–4]. For those studies on materials that do not have structural anisotropy, templating approaches[13] (in porous alumina) have been generally used, which result in predominantly amorphous or polycrystalline tubes[5]. In the process we report here, an 'epitaxial casting' approach was taken. Hexagonal-shaped single-crystal ZnO nanowires are used as templates initially during the GaN deposition (Fig. 3). As ZnO and GaN both have wurtzite crystal structures and have similar lattice constants (ZnO: $a = 3.249$ Å, $c = 5.207$ Å; GaN: $a = 3.189$ Å, $c = 5.185$ Å), GaN can grow epitaxially on the side {110} planes of these ZnO nanocylinders and form a thin single-crystal GaN layer. Once the ZnO nanocylinders were coated with a thin GaN sheath, they were subsequently removed by thermal processes. There are two possible mechanisms for the removal of ZnO templates. First, ZnO can be chemically etched by ammonia at high temperature[14]. Prolonged heating of samples after GaN coating in NH_3 readily yields pure GaN nanotubes. The other approach is to use thermal reduction at high temperatures (for example, 600 °C in H_2). The single-crystal wurtzite GaN nanotubes reported here differ fundamentally from theoretically simulated GaN nanotubes, where a metastable graphitic GaN structure was proposed[15].

We have confirmed this 'epitaxial casting' mechanism by TEM studies. Arrays of GaN nanotubes with their ZnO nanowire templates partially removed are shown in Fig. 4a, b. Note that there is a thin layer of porous GaN film at the bottom of these nanotubes. In addition, the residue ZnO nanowire templates remain in the upper portion of the sealed GaN nanotubes. These two observations suggest that the zinc and oxygen species (generated during the thermal chemical etching process) escape from the GaN nanotubes primarily through the porous GaN layer (Supplementary Information). Electron diffraction (Fig. 4b insets) shows an identical set of diffraction pattern for both the tube and the core–sheath region, indicating the wurtzite GaN growth is epitaxial. The core–sheath nanostructure can be considered as a seamless single domain of a wurtzite GaN/ZnO structure type. Furthermore, comparison of EDX line profiles across the GaN nanotube (Fig. 4d) and the ZnO–GaN core–sheath structure (Fig. 4c) unambiguously supports the growth mechanism of GaN nanotube on the ZnO nanowire templates. Once the ZnO nanocylinder is removed, single-crystal tubes of GaN result. To the best of our knowledge, this is the first example of the formation of single-crystal GaN nanotubes. (There was a previous report on GaN nanotube formation, but those tubes were highly irregular and polycrystalline[16].) We note that microscale tubes of ZnO have been prepared in solution through a preferential chemical dissolution process[17].

The electrical and optical characteristics of these single-crystal GaN nanotubes are comparable to those of high-quality GaN epilayers grown on ZnO substrates[18], as well as those of GaN nanowires[19,20]. We measured low-temperature photoluminescence spectra of our nanotubes using fourth-harmonic output of a YAG

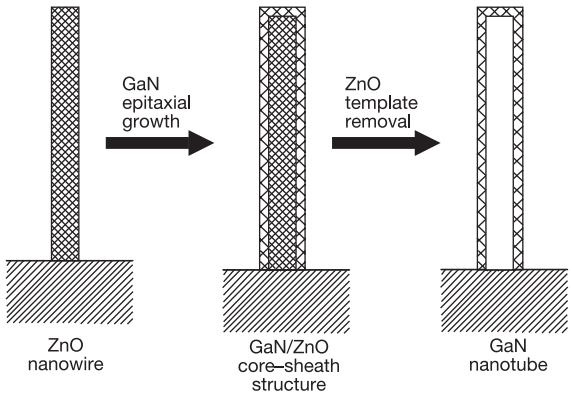

Figure 3 Schematic illustration of the 'epitaxial casting' process for making single-crystal GaN nanotubes.

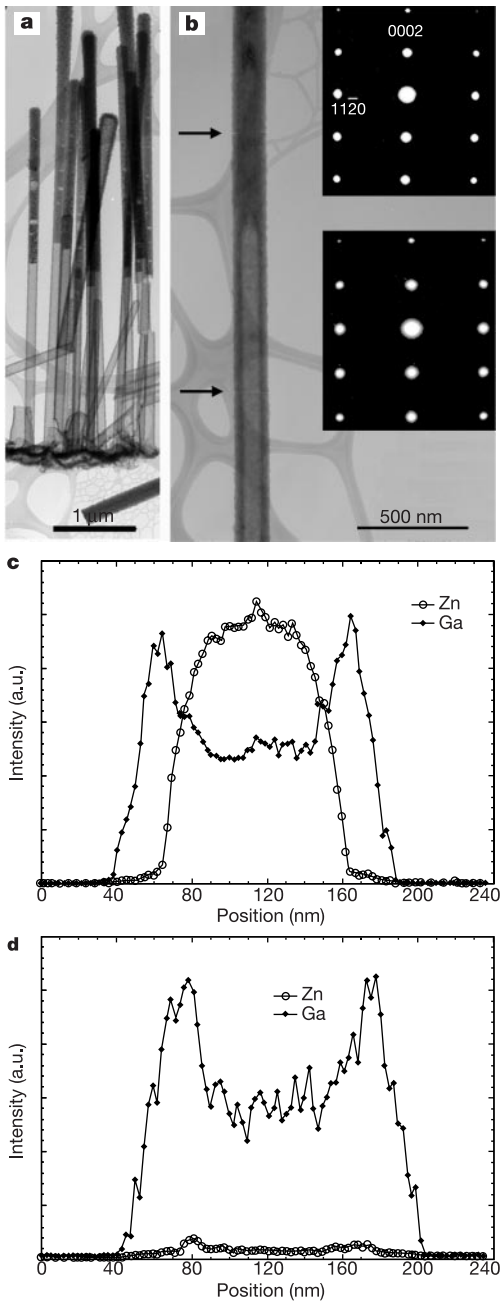

Figure 4 Characterization of the interface between the GaN tube and the ZnO wire. **a**, **b**, TEM images of arrays of GaN nanotubes with their ZnO nanowire templates partially removed. Insets in **b** are electron-diffraction patterns recorded on the core–sheath and the pure tube region along the [1̄10] zone axis. **c**, **d**, Compositional (Ga and Zn signals) line profiles for core–sheath GaN/ZnO (**c**) and the GaN tube region (**d**) indicated by upper and lower arrows in **b**, respectively.

laser (266 nm) as excitation source. No midgap yellow emission was observed. Band-edge emission was observed in these nanotube samples between 375 and 360 nm, with the thinner tubes emitting at shorter wavelengths (Supplementary Information). This slight blueshift of the emission[18] could be attributed to the quantum confinement effect, as some of the nanotubes have walls as thin as 5 nm, which is smaller than the exciton Bohr radius of GaN. Electron transport measurements indicate the resistances of these nanotubes are of the order of 10 MΩ at room temperature, and increase with decreasing temperature (Supplementary Information), similar to those of high-quality GaN nanowires[19,20].

The semiconductor nanotubes that we report here are mechanically robust, and electrically and optically active. They could therefore offer opportunities for further fundamental research, as well as for technological applications in nanocapillary electrophoresis, nanofluidic biochemical sensing, nanoscale electronics and optoelectronics[21]. The successful preparation of single-crystal GaN nanotubes using this 'epitaxial casting' approach suggests that it is possible to prepare single-crystal nanotubes of other inorganic solids that have non-layered crystal structures[22,23]. □

Received 14 November 2002; accepted 26 February 2003; doi:10.1038/nature01551.

1. Iijima, S. Helical microtubules of graphitic carbon. *Nature* **354,** 56–58 (1991).
2. Tenne, R. & Zettl, A. K. Nanotubes from inorganic materials. *Top. Appl. Phys.* **80,** 81–112 (2001).
3. Tenne, R. Inorganic nanoclusters with fullerene-like structure and nanotubes. *Prog. Inorg. Chem.* **50,** 269–315 (2001).
4. Patzke, G. R., Krumeich, F. & Nesper, R. Oxidic nanotubes and nanorods—Anisotropic modules for a future nanotechnology. *Angew. Chem. Int. Edn Engl.* **41,** 2446–2461 (2002).
5. Martin, C. R. Nanomaterials—a membrane-based synthetic approach. *Science* **266,** 1961–1965 (1994).
6. Ajayan, P. M. *et al.* Carbon nanotubes as removable templates for metal-oxide nanocomposites and nanostructures. *Nature* **375,** 564–566 (1996).
7. Yang, S. M. *et al.* Formation of hollow helicoids in mesoporous silica: Supramolecular origami. *Adv. Mater.* **11,** 1427–1430 (1999).
8. Kondo, Y. & Takanayagi, K. Synthesis and characterization of helical multi-shell gold nanowires. *Science* **289,** 606–608 (2000).
9. Li, Y. *et al.* Bismuth nanotubes. *J. Am. Chem. Soc.* **123,** 9904–9905 (2001).
10. Wu, Y. & Yang, P. Melting and welding semiconductor nanowires in nanotubes. *Adv. Mater.* **13,** 520–523 (2001).
11. Schmidt, O. G. & Eberl, K. Thin solid films roll up into nanotubes. *Nature* **410,** 168 (2001).
12. Huang, M. *et al.* Room-temperature ultraviolet nanowire nanolasers. *Science* **292,** 1897–1899 (2001).
13. Caruso, R. A. & Antonietti, M. Sol-gel nanocoating: an approach to the preparation of structured materials. *Chem. Mater.* **13,** 3272–3282 (2001).
14. Hamdani, F. *et al.* Effect of buffer layer and substrate surface polarity on the growth by molecular beam epitaxy of GaN on ZnO. *Appl. Phys. Lett.* **71,** 3111–3113 (1997).
15. Lee, S. M. *et al.* Stability and electronic structure of GaN nanotubes from density-functional calculations. *Phys. Rev. B* **60,** 7788–7791 (1999).
16. Li, J. Y. *et al.* Synthesis of GaN nanotubes. *J. Mater. Sci. Lett.* **20,** 1987–1988 (2001).
17. Vayssieres, L., Keis, K., Hagfeldt, A. & Lindquist, S. Three-dimensional array of highly oriented crystalline ZnO microtubes. *Chem. Mater.* **13,** 4395–4398 (2001).
18. Hamdani, F. *et al.* Microstructure and optical properties of epitaxial GaN on ZnO (0001) grown by reactive molecular beam epitaxy. *J. Appl. Phys.* **83,** 983–990 (1998).
19. Huang, Y., Duan, X., Cui, Y. & Lieber, C. M. Gallium nitride nanowire nanodevices. *Nano Lett.* **2,** 101–104 (2002).
20. Kim, J. *et al.* Electrical transport properties of individual gallium nitride nanowires synthesized by chemical vapor deposition. *Appl. Phys. Lett.* **80,** 3548–3550 (2002).
21. Schoening, M. & Poghossian, A. Recent advances in biologically sensitive field-effect transistors (BioFETs). *Analyst* **127,** 1137–1151 (2002).
22. Lauhon, L. J., Gudiksen, M. S., Wang, D. & Lieber, C. M. Epitaxial core-shell and core-multishell nanowire heterostructures. *Nature* **420,** 57–61 (2002).
23. He, R., Law, M., Fan, R., Kim, F. & Yang, P. Functional bimorph composite nanotapes. *Nano Lett.* **2,** 1109–1112 (2002).

Supplementary Information accompanies the paper on *Nature*'s website (http://www.nature.com/nature).

Acknowledgements We thank the National Center for Electron Microscopy for the use of their facilities. This work was supported by the Camille and Henry Dreyfus Foundation, the Research Corporation, the Hellman Family Faculty Foundation and the Beckman Foundation. J.G. thanks the National Science Foundation for Graduate Fellowship support. P.Y. is an Alfred P. Sloan Research Fellow. Work at the Lawrence Berkeley National Laboratory was supported by the Office of Science, Basic Energy Sciences, Division of Materials Science of the US Department of Energy.

Competing interests statement The authors declare that they have no competing financial interests.

Correspondence and requests for materials should be addressed to P.Y. (e-mail: p_yang@uclink.berkeley.edu).

Deep roots of the Messinian salinity crisis

Svend Duggen*†, Kaj Hoernle*, Paul van den Bogaard*, Lars Rüpke* & Jason Phipps Morgan*

** GEOMAR Research Center for Marine Geosciences, Wischhofstrasse 1-3, 24148 Kiel, Germany*

The Messinian salinity crisis—the desiccation of the Mediterranean Sea between 5.96 and 5.33 million years (Myr) ago[1]—was one of the most dramatic events on Earth during the Cenozoic era[2]. It resulted from the closure of marine gateways between the Atlantic Ocean and the Mediterranean Sea, the causes of which remain enigmatic. Here we use the age and composition of volcanic rocks to reconstruct the geodynamic evolution of the westernmost Mediterranean from the Middle Miocene epoch to the Pleistocene epoch (about 12.1–0.65 Myr ago). Our data show that a marked shift in the geochemistry of mantle-derived volcanic rocks, reflecting a change from subduction-related to intraplate-type volcanism, occurred between 6.3 and 4.8 Myr ago, largely synchronous with the Messinian salinity crisis. Using a thermomechanical model, we show that westward roll back of subducted Tethys oceanic lithosphere and associated asthenospheric upwelling provides a plausible mechanism for producing the shift in magma chemistry and the necessary uplift (~1 km) along the African and Iberian continental margins to close the Miocene marine gateways, thereby causing the Messinian salinity crisis.

In the Late Miocene (~8 Myr ago), marine passages in southern Spain and northern Morocco linked the Mediterranean Sea to the Atlantic Ocean (Fig. 1). The palaeodepth of the Rifean corridor in Morocco—the deepest of these gateways—was estimated at 600–800 m (refs 3, 4). Marine sediments, such as terraced reef complexes from these former channels, now outcrop several hundred metres above sea level[5,6]. Three possible mechanisms have been proposed to close these marine passages: (1) global sea level drop of ~60 m (refs 7, 8); (2) horizontal shortening associated with crustal nappe movements[9]; and (3) tectonic uplift[3,4,10].

Not only was the ~60-m drop in sea level in the Messinian insufficient to have closed all of the Late Miocene marine gateways, but also it has recently been shown that the onset of evaporite deposition at 5.96 ± 0.02 Myr does not correspond to the open-ocean benthic $\delta^{18}O$ signal, which is commonly interpreted to reflect glacio-eustatic sea-level changes. Therefore a global sea-level drop cannot have caused the Messinian salinity crisis (MSC)[1,11]. Horizontal shortening is also an unlikely mechanism, for two reasons. First, because emplacement of crustal nappes in the Early Miocene, connected with extensional collapse of the Alborán block thickened through the collision of Africa and Iberia[12], had already ceased before the Late Miocene in the Betics[13], and second, there is no evidence that nappe emplacement blocked the Rifean corridor in the Late Miocene (Fig. 1)[3]. It has, however, been shown that sediments in the former marine gateways were uplifted in the Late Miocene and Pliocene to their present elevations[3,5,10]. Palaeodepth reconstructions indicate a rapid shallowing in the Late Miocene with rates as high as 5 mm yr^{-1} at 7.2 Myr ago in the southern Rifean corridor, which was emergent by ~6.0 Myr (ref. 3). An increase of continental detritus in the uppermost Pliocene deposits of the Alborán basin indicates a continuation of this uplift into the Pliocene[14].

† Present address: Department of Geology, Royal Holloway University of London, Egham, Surrey TW20 0EX, UK.